SAND2022-4449C

The 10th International Conference on Modeling and Diagnostics for Advanced Engine Systems (COMODIA 2022), July 5-8, 2022, Sapporo, Japan

#0141

High-speed low-coherence interferometry for film thickness measurements in impinging gasoline direct injection sprays

*Logan White, Julien Manin, and Lyle M. Pickett

Combustion Research Facility, Sandia National Laboratories
7011 East Ave, Livermore, CA 94550, USA

Key Words: Interferometry, Fuel Films, GDI, Wall Wetting, Impinging Sprays

ABSTRACT

Wall impingement and fuel film deposition in gasoline direct injection engines under cold start conditions are major concerns for emissions reduction. However, it is challenging to study the dynamics of film deposition under realistic conditions because of the difficulty of measuring the thicknesses of these microscale films. Low-coherence interferometry provides a quantitative optical film thickness measurement technique that can be applied to study this problem. This work presents the first high-speed spectral low-coherence interferometry measurements of impinging gasoline direct injection sprays. The feasibility and practical concerns associated with high-speed low-coherence interferometry systems are explored. Two approaches to spectral low-coherence interferometry: Michelson interferometry and Fizeau interferometry, were implemented and are compared. The results show that Fizeau interferometry is the better option for measurements of impinging sprays in closed spray vessels. The high-speed low-coherence interferometry system was applied in the Fizeau configuration to measure time-resolved film thickness of impinging sprays under engine-relevant conditions to demonstrate its capabilities.

INTRODUCTION

Gasoline Direct Injection (GDI) technology offers gains in the efficiency of Internal Combustion Engines (ICEs) of passenger vehicles but also comes with the risk of wetting combustion chamber surfaces, especially at cold start. Pool fires on wetted surfaces in ICEs have been linked to high-soot events that can significantly impact emissions performance [1,2,3]. Wall wetting has also been linked to oil dilution and reduced engine component lifetimes [4]. To improve on the current state of understanding of these film formation processes, it is important to be able to measure fuel film thicknesses under engine-relevant conditions. An improved understanding of film dynamics will allow for the development of better computational models that can be used for research and the design of high-efficiency engines.

Prior experimental efforts investigating impinging sprays have used a variety of optical techniques to measure film thickness with transparent walls. Several prior efforts leveraged Laser-Induced Fluorescence (LIF) from fuel tracer species such as toluene [5] and 3-pentanone [6]. These techniques exhibit high sensitivity, but their interpretation is complicated by the dependence on temperature and oxygen concentration. An alternative approach has been to target similar species with extinction illuminated by either a laser [7] or a UV Light-Emitting Diode (LED) [8]. Both LIF and extinction techniques require calibration and/or accurate photophysical modeling to infer the actual film thickness. Because they target specific chemical species in the fuel mix, they are susceptible to the effect of preferential evaporation in the spray and film. Additionally, these techniques are sensitive to fuel in the form of droplets and vapor above the surface of the fuel, which can confound results. Ultimately, these optical methods would benefit from corroboration with a technique that is less susceptible to confounding factors and that can be more directly quantified.

This work explores the application of Low Coherence Interferometry (LCI) as an alternative method for performing high-speed quantitative measurements of fuel film thicknesses. LCI offers these attributes as it is fundamentally a measure of optical transit time through the film. LCI uses a broadband light source to compare light that has traveled along different optical paths to infer the relative distances of those two paths. The use of broadband illumination reduces the coherence length of the light to micrometer scales. This eliminates what is known as 2π ambiguity, an uncertainty in signal interpretation that can exist in monochromatic laser interferometry, where the coherence length can be on the order of 100 m. LCI is advantageous for fuel film measurements because it can be readily quantified without the need for calibration. It is also more robust to spurious

influences as it exhibits a limited dependence on temperature and is insensitive to droplets and vapor above the film.

This work focuses on spectral LCI, where the interference signal is detected using a spectrometer to infer information from spectral interference patterns. For thin film measurements, there are two interferometer configurations that are typically implemented: Michelson interferometry and Fizeau interferometry. A Michelson interferometer uses a *reference* mirror in a separate optical path to determine the relative position of the gas-liquid interface of the film. A Fizeau interferometer uses the relative path difference between the gas-liquid and liquid-wall interfaces of the film to generate the interference signal. In this work, both configurations were tested and compared.

Initial work toward measuring the thickness of dynamic liquid films using LCI was undertaken by Borgetto et al. [9]. These experiments implemented time-domain LCI in the Michelson configuration to monitor falling liquid films with thicknesses on the order of 50 µm. The results demonstrated precise film thickness determination, but the time-domain approach is not capable of the temporal resolution necessary for GDI measurements. Schumacher et al. [10] implemented a dual imaging interferometry approach to study impinging Diesel sprays in a constant volume spray chamber. That work included a Fizeau type spectral LCI measurement illuminated by a high-power xenon lamp. The low-ambiguity spectral LCI measurements were made along a one-dimensional axis across the spray footprint that could then be correlated with two-dimensional Fizeau interferometry images to produce two-dimensional film thickness measurements. However, the relatively low intensity of the xenon lamp required long exposure times and therefore precluded temporal resolution and high frame rates in the spectrally resolved channel.

This work aims to extend the use of high-accuracy spectral LCI to high-speed measurements that can resolve film dynamics of impinging sprays. Both Michelson and Fizeau interferometer configurations were tested to compare their effectiveness in practical spray chamber tests at engine-relevant conditions. The Methods section describes the theoretical aspects of LCI that are important to design and essential details of the system's practical implementation. The Results section presents the application of the high-speed LCI system to study impinging GDI sprays in a constant volume spray chamber under cold start conditions.

EXPERIMENTAL METHOD

LCI basics and theory

Interferometry encompasses a family of optical measurement techniques that infer properties of a system by comparing light that has traveled along two separate optical paths. The interaction of the two combined light beams produces an interference pattern that is detected by a sensor. This work focuses on LCI, where the light source exhibits a short coherence length by emitting over a broad spectrum of wavelengths. The coherence length of a light source with a Gaussian spectrum can be expressed as:

$$l_c = \frac{2\ln(2)}{\pi}\frac{\lambda_0^2}{\Delta\lambda} \quad (1)$$

where λ_0 is the central wavelength and $\Delta\lambda$ is the Full Width at Half-Maximum (FWHM). Specifically, this work applies spectral (also known as Fourier-domain) LCI, where the detected signal is spectrally resolved, and information is inferred by analyzing interference patterns in the measured spectrum. Spectral LCI is advantageous for high-speed measurements because depth information can be captured in a single-shot manner, while the alternative time-domain methods require scanning the measurement in time [11].

An LCI system comprises a broadband light source, a beam splitter to guide the light along one or more paths and recombine them, and a detector at the output port of the beam splitter (see Fig. 1). In principle, a spectral LCI system detects reflections of light from surfaces and senses how they are distributed in optical path length. A general analysis of interferometric theory can be applied to potentially complicated systems to predict what signals might be produced. The case of a liquid film back-illuminated through a transparent wall can be treated very simply as two reflecting surfaces: the *sample* surface at the gas-liquid interface of the film and the *reference* surface to which it is compared. The source of the *reference* reflection determines the type of interferometry, Michelson or Fizeau (to be discussed below), but precise measurement of the *sample* surface location relative to a known wall position is sufficient to determine the film thickness.

In this two-surface case, the spectrum measured at the interferometer detector, I(k), can be expressed as [11]:

$$I(k) = (r_R + r_S)I_0(k) + \sqrt{r_R r_S}I_0(k)\cos(2n_F k\Delta z) \quad (2)$$

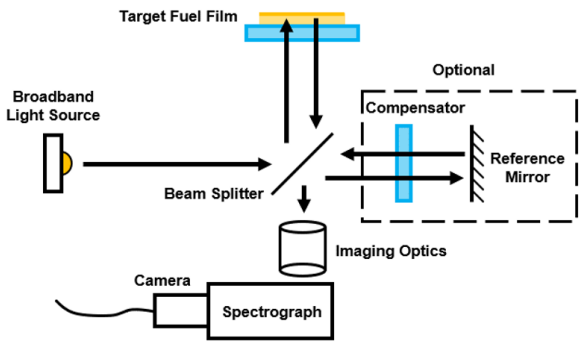

Fig. 1 Schematic showing the basic components of a typical LCI system.

where $I_0(k)$ is the source's emitted spectrum, r_R is the reflectivity coefficient of the *reference* surface, r_S is the reflectivity coefficient of the *sample* surface, n_F is the index of refraction of the fuel, and Δz is the difference in distances to the *reference* and *sample* surfaces. Note that the spectral dependence is represented in angular wavenumber, $k = 2\pi/\lambda$. The path difference, Δz, is the value of interest, and it can be extracted by performing a Fourier transform of the measured spectrum. This Fourier domain representation, referred to in this work as the scattering potential [11], can be expressed as:

$$F(z') = (r_R + r_S)\mathcal{F}\{I_0(k)\} + \sqrt{r_R r_S}\mathcal{F}\{I_0(k)\} * [\delta(z' - 2n_F\Delta z) + \delta(z' + 2n_F\Delta z)] \quad (3)$$

Where $\mathcal{F}\{I_0(k)\}$ is the Fourier transform of the source spectrum, z' is the Fourier domain variable, and δ represents the Dirac delta function. The $*$ operator represents a convolution between the peaks representing the path difference and the Fourier transform of the source spectrum (the significance of this is discussed below). In this way, the path difference can be extracted by identifying the peak in the Fourier transform of the measured spectrum. Note that the technique retains a dependence on temperature and composition of the fuel film through the index of refraction factor that must be known when interpreting the results. However, this variation is typically <5% for most conditions and is a significant improvement over the confounding effects experienced by LIF and extinction measurements. The first term in Eq. (3) conveys no information about the film thickness and will be referred to as the DC component because it is centered at the zero frequency.

Spatial resolution becomes critical in LCI for reasons beyond just localizing the measured signal in space. In fact, the LCI signal will disappear or "wash-out" if the optical setup fails to achieve sufficient spatial resolution when measuring films of nonuniform thickness. This can be explained by considering a flat fuel film surface that exists at an angle relative to the *reference* surface that it is being compared to with the interferometer. If the optical projection of the detector pixel through the imaging optics onto the portion of the film that it is observing is considered, then the spectral fringes can be seen to change across the width of the projected pixel due to the varying path length to the film surface. If the difference in fringe phase changes significantly (by π radians or more) across the projected pixel, then the fringes will cancel out when integrated across the pixel, leading to a loss of signal (wash-out).

For this reason, the spatial resolution of the optical setup limits the maximum angle at which the fuel film can be inclined relative to the *reference* surface and still be detected. Schumacher et al. [10] show that the maximum detectable angle, α_{max}, can be expressed as:

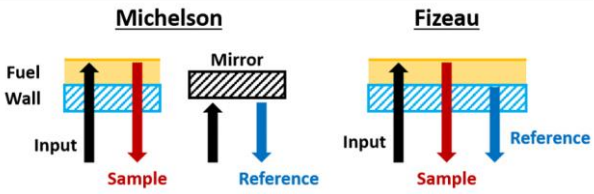

Fig. 2 The difference between Michelson and Fizeau interferometry is based on the origin of the *reference* reflection.

$$\alpha_{max} = \tan^{-1}\left(\frac{\lambda}{2n_F d_{min}}\right) \quad (4)$$

where d_{min} is the smallest resolvable point separation of the optical system. This can have important implications in the design of an LCI system for impinging sprays. Initial spray impingement produces a chaotic and highly corrugated film surface. Additionally, after the initial film deposition, the hydrodynamics of additional spray droplets impacting the fuel film can promote corrugation of the film. The steep angles of this corrugated surface prevent quantitative thickness measurements with LCI until the film settles (through surface tension effects) such that the typical surface angles are below the α_{max} value determined by the optical setup. In this way, it is desirable to pursue the finest possible spatial resolution to enable the earliest possible thickness measurements of the dynamic film. This can present a design tradeoff in systems that are limited by minimum Signal-to-Noise Ratio (SNR) constraints such that increasing the spatial resolution could reduce the collected light intensity below a critical value.

Types of interferometry: Michelson versus Fizeau

One of the main goals of this study is to compare the effectiveness of the Michelson and Fizeau interferometer configurations for film measurements in spray vessels. The main difference between the two approaches is where the *reference* light path is generated. In Michelson interferometry, a separate *reference* mirror is used to reflect light in a separate "arm" of the interferometer. The mirror is positioned at approximately the same distance from the beam splitter as the target liquid-gas interface. Advantages of this configuration include a higher SNR (although the *reference* mirror reflectivity was not optimized for maximum SNR in this study) and fewer constraints on the material used for the transparent wall (Fizeau interferometry needs to avoid refractive index matching between the fuel and the wall material). However, significant disadvantages include the need for precise dispersion correction in the *reference* light path and for the transparent wall position to be well-known and static (no recoil) throughout the injection test.

In Fizeau interferometry, the *reference* light path is produced by the liquid-wall interface due to a refractive index mismatch between the fuel and transparent wall material. For this reason, an appropriate material must be

chosen. In the case of the gasoline surrogates, that must be a high refractive index material; sapphire was chosen in this work. The Fizeau configuration requires a simpler setup and less precise optical alignment compared to Michelson interferometry. Critically, the Fizeau approach is insensitive to any motion or recoil of the transparent wall because it directly measures the relationship between the film surface and the wall. The biggest drawback of Fizeau interferometry is that both reflection sources are typically weak and lead to lower SNRs.

Dispersion is an important aspect to consider in the implementation of an LCI system. Dispersion describes the effects experienced by light propagating through a medium with a wavelength-dependent index of refraction, as is the case with virtually all media. This causes the phase of different wavelengths to become desynchronized such that it appears that each wavelength experiences a different path length when measured by its phase. The upshot is that if the *reference* and *sample* paths of an LCI system have different dispersion properties, this will lead to a loss of depth resolution due to a deviation from the wavelength independence of the refractive index that is implicitly assumed in Eq. (2). This makes it critical to match the total dispersion through all the media in both the *reference* and *sample* paths.

In Fizeau interferometry, the *reference* optical path is almost identical to the *sample* optical path because they travel collinearly up to the wall-liquid interface. This makes the dispersion experienced by both beams the same except for dispersion of the *sample* beam while transiting through the fuel film. Because the fuel film is generally thin (≤ 20 μm), the dispersion effects are negligible, and Fizeau interferometry is naturally unaffected by dispersion in spray measurements. For Michelson interferometry, the *reference* optical path is completely separated from that of the *sample* path going to the film. The dispersion contributions from all media in the *sample* path must be recreated in the *reference* path to rectify the effects of dispersion in this configuration. For spray vessel measurements, this includes placing replicas of the thick pressure windows, the transparent walls, and the beam splitter into the *reference* path.

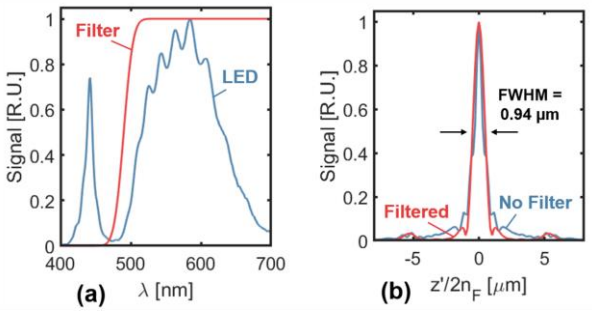

Fig. 3 (a) White phosphor LED (Cree XHP35) emission spectrum (b) Fourier transform of white LED spectrum (transformed into z' coordinates).

Practical concerns for LCI systems and current design

The performance of the illumination source is critical to determining the capabilities of an LCI system. The primary influence is that the spectral bandwidth of the light source determines the thickness resolution that can be achieved. The FWHM of a peak in the scattering potential corresponding to a surface can be expressed as a function of the coherence length:

$$\Delta z_{\mathrm{FWHM}} = \frac{l_c}{n_{\mathrm{F}}} = \frac{2\ln(2)}{\pi n_{\mathrm{F}}} \frac{\lambda_0^2}{\Delta\lambda} \tag{4}$$

This shows that maximizing the bandwidth of the source is necessary to achieving optimal resolution of the film thickness.

While previous LCI implementations have used gas discharge lamps and superluminescent diodes [10], these sources have important limitations hampering their use for high-speed, high-resolution systems. Gas discharge lamps, such as xenon and mercury lamps, provide high bandwidths but lower spectral intensities that would require longer integration times to achieve usable SNRs. Superluminescent diodes offer more intensity but typically have narrower spectral bandwidths. A promising alternative source is white phosphor LEDs that can be pulsed to produce sufficient intensities for single-shot LCI measurements.

White phosphor LEDs use a blue pump LED to excite a phosphor emitter layer that fluoresces to produce a broadband visible emission spectrum. This blue pump light also leaks through the phosphor layer and produces a short wavelength peak. An example spectrum generated by the Cree XHP35 LEDs used in this system is shown in Fig. 3. When analyzing the collected data, the blue peak was filtered out during post-processing using the filter shown in Fig. 3(a). This was done to narrow the width of the Fourier domain representation of the light source, as shown in Fig. 3(b). It is this Fourier domain distribution that is superimposed on measured peaks in the scattering potential and determines system resolution. This was computed using a fuel refractive index of 1.413 (that of the fuel described below) and shows that the expected thickness resolution limit of the system is 0.94 μm (FWHM). The small peaks in the profiles shown in Fig. 3(b) near 5.5 μm are the result of the oscillations in spectral intensity superimposed on the approximately Gaussian distribution in Fig. 3(a). These are not a feature of the LED but instead are an artifact of the high-speed CMOS camera's spectral response.

A key consideration in the implementation of high-speed pulsing of LEDs is thermal management. As the LED is pulsed at high power, the heat dissipated by the die increases the temperature of the die and the rest of the LED package. Subsequent pulses continue to heat the LED die, and if it exceeds a critical safe temperature, then thermal failure mechanisms become likely. Testing showed that the pulse parameters required for sufficient

SNRs (30 V forward voltage and a 15 µs pulse at 10 kHz) produced thermal failure of the LED in less than 20 pulses when the die is initially at room temperature. This occurs despite a large aluminum heat sink with a cooling fan thermally bonded to the LED package. The heat dissipated in the die accumulates within the package more rapidly than it can be removed to the heat sink.

This was addressed in this implementation by using a Peltier-type ThermoElectric Cooler (TEC) to cool the LED die to sub-ambient temperatures. This both provides increased thermal headroom below the critical die temperature and increases the heat transfer rate out of the die and package. The TEC used was rated to a maximum heat removal rate of 108 W and was operated at a current of 3.5 A to achieve LED package temperatures between -20°C to -25°C. Under these conditions, the LED could be pulsed up to 1000 times per injection and was able to survive for between 5 to 100 injections before thermal failure occurred. All tested LEDs eventually reached failure, showing that this implementation reached the limits of this LED model's performance.

The signal was detected with spectral resolution using a high-speed CMOS camera (Photoron SA-X2) coupled to a 320 mm focal length imaging spectrograph (Princeton Instruments Isoplane SCT 320). The spectrograph provided one dimension of spatial resolution along its vertically oriented entrance slit. The spectrograph can be reconfigured to use different diffraction gratings on the fly using a rotating grating turret. In this work, some benchtop calibration tests used a 150 lines/mm grating (0.19 nm per pixel), but all the spray vessel measurements in the Results section used a 50 lines/mm grating (1.12 nm per pixel). The coarser grating was used in those tests to increase the spectral light intensity reaching the sensor to maintain an adequate SNR. A lack of spectral resolution can limit the maximum film thickness that an LCI system can resolve, but this was not an issue in this study of the relatively thin GDI films.

As discussed above, the imaging optics chosen for a system are important as the spatial resolution they achieve limits the maximum detectable film angle. For benchtop tests, this parameter was not critical, and so 50 mm or 105 mm focal length camera lenses were used for those tests. For tests in the spray chamber using the Michelson configuration, a 200 mm f/4 camera lens was used to achieve a projected pixel size of 32.8 µm. Taking this projected pixel size as an optimistic limit of minimum resolvable distance yields an estimated maximum film angle of 0.34° for the Michelson setup. The resolution of the imaging setup was improved for the subsequent Fizeau setup (based on findings from the Michelson tests) by using a three-piece combination of a 105 mm f/1.8 lens, a 20x Mitutoyo APO, and a 50 mm Nikkor lens. This produced a projected pixel size of 11.6 µm, which corresponds to an optimistic estimate of 0.96° for the maximum film angle.

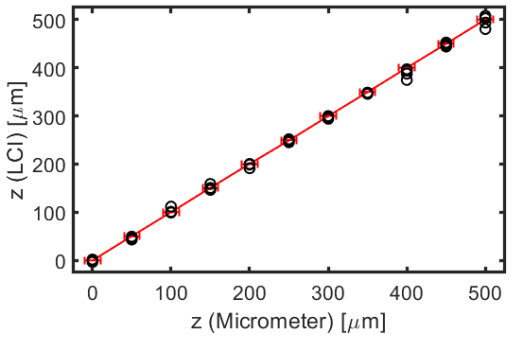

Fig. 4 A comparison of the LCI measured and micrometer measured mirror locations.

Preliminary benchtop tests

Benchtop tests were performed to confirm the feasibility and accuracy of the high-speed LCI system. These included a confirmation of the accuracy of the system's depth measurements and a test of the system's response to liquid films.

A simple test was performed using two mirrors to gauge the accuracy of depth measurements with the LCI system. The LCI system was set up in the Michelson configuration such that there was one high-reflectivity mirror in the *reference* path and another high-reflectivity mirror in the *sample* path, although the *reference-sample* distinction was irrelevant in this case. The positions of the mirrors were adjusted until the interference signal was detected. One of the mirrors was then translated at fixed intervals using a micrometer-driven translation stage at increments of 50 µm (5 µm uncertainty), and LCI measurements of the relative positions were captured. The scattering potentials were computed by taking the Fourier transform of the wavenumber-space representation of the measured spectra at several spatial locations. Fig. 4 shows a comparison of the position measured by LCI (scattering potential peak) with the target position of the translation

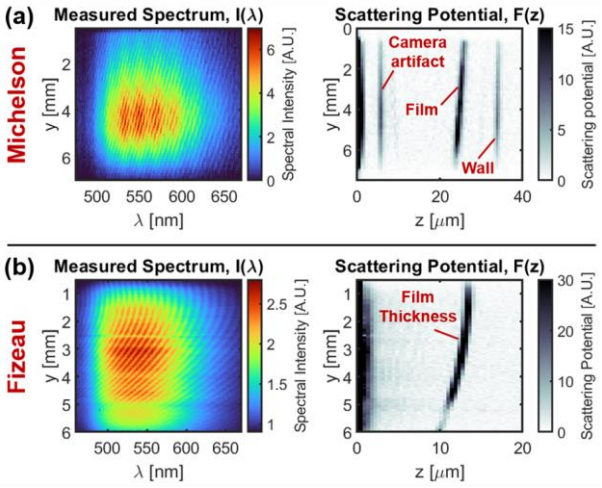

Fig. 5 Film thickness measurements of (a) A falling iso-octane film with the Michelson configuration (b) An evaporating iso-octane film with the Fizeau configuration.

stage. The LCI measurements recover the position of the mirror to within the translation stage's positional uncertainty. This demonstrates the accuracy of the relative depth positioning measured by the LCI system.

To test the capability of the LCI system to measure liquid film thicknesses, experiments observing falling and evaporating liquid films were performed. In these tests, liquid iso-octane was applied from an eyedropper onto either a vertical or horizontal glass slide on an open-air mount. It was not possible to precisely control the resulting film thickness or measure it with greater precision than the LCI system, and so the main purpose of these measurements was to confirm the feasibility of time-resolved liquid film measurements with this system. Fig. 5 shows raw image measurements and scattering potentials for each interferometry type. In the raw images, the horizontal axis is wavelength as dispersed by the spectrometer and the vertical axis is the spatial location, denoted by y, resolved by the optics. In the scattering potential images, the vertical axis is again spatial location and the horizontal axis is distance normal to the wall (the thickness dimension).

To extract quantitative fuel film thickness measurements from the Michelson interferometry, it is necessary to compare the locations of the transparent wall and the fuel film surface in the scattering potential. The difference in the depth coordinate, $z = z'/2n_F$, where the peaks in the scattering potential are observed gives the film thickness. Fig. 5(a) shows the captured interferometry frame and the corresponding scattering potential computed by taking a line-by-line Fourier transform of the spectrum at each y location. The scattering potential shows the measurement's DC component at $z = 0$ as well as the camera artifact near 5.5 µm. The peak associated with the film surface is observed between 24 to 26 µm and the peak associated with the transparent wall is observed near 34 µm. This indicates a film thickness between 8 to 10 µm over the spatial extent of the Michelson measurement. Both peaks exhibit a Gaussian-fitted FWHM of approximately 1 µm, consistent with the bandwidth of the light source. This indicates that the dispersion due to the glass slide and beam splitter was adequately compensated by the optics installed in the *reference* path.

For Fizeau interferometry, the film thickness is directly recovered from the single peak observed at each spatial location in the scattering potential. Because the signal is generated from the interference of light reflecting from the wall and film surfaces, the measurement directly probes their relative separation. Fig. 5(b) shows an example Fizeau measurement of an evaporating iso-octane film. The measured spectrum clearly shows the periodic spectral intensity variation that encodes information about film thickness. The scattering potential shows a single peak at each location corresponding to the apparent film thickness. In this observation, the film thickness varied between 10 to 13 µm over the spatial extent of the measurement. The camera artifact seen in Fig. 5(a) is absent in this example because a different camera (low-speed CCD) was used to record this measurement. The FWHM of the scattering potential peaks was also approximately 1 µm in these Fizeau measurements. This high resolution is expected because the Fizeau configuration inherently provides near-perfect dispersion compensation.

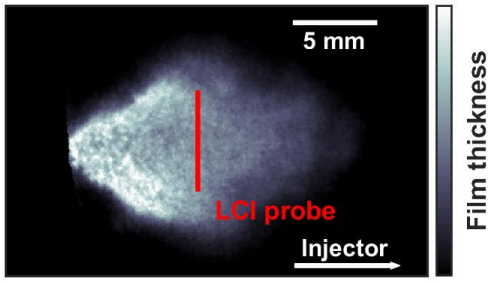

Fig. 7 Location of LCI measurements relative to LIF image of impinging spray footprint.

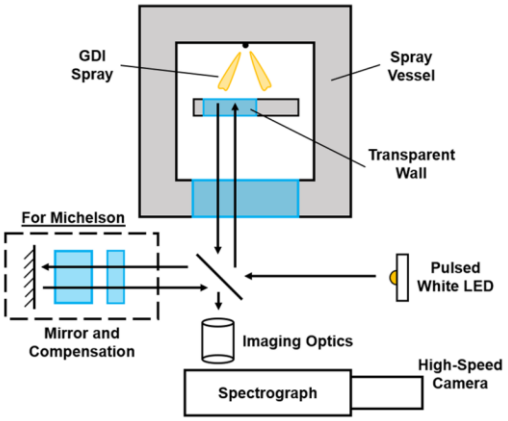

Fig. 6 Schematic showing the experimental setup used for measurements in the spray vessel.

Experimental setup for spray vessel tests

The engine condition tests were performed in a constant volume spray vessel [12]. The chamber has a cubic internal volume of 1 L and provides optical access through 48 mm thick sapphire pressure windows from all orthogonal views around the injector. The pressure and composition of the gas within the chamber are controlled by a gas delivery system. The temperature of the chamber is controlled by a system of heaters and insulation built around the chamber walls. For the trials in this work, the chamber was operated at a pressure of 1 bar and two temperature conditions: 20°C (cold condition) or 90°C (hot condition). The injector used for the tests was an ECN spray G GDI injector with a symmetric 8-hole spray pattern. All tests were performed with an LED pulsing and acquisition rate of 10 kHz.

The wall position for all impinging spray tests was 40 mm downstream of the injector tip. This position was chosen to be representative of the piston crown location during intake-stroke injection in a typical GDI engine (310 CAD bTDC for engine in [13]). The transparent wall was made of either a 7.75 mm thick piece of fused silica (Michelson

measurements) or a 5 mm thick piece of sapphire (Fizeau measurements). The transparent piece was held by a custom-designed aluminum retainer with a 50 mm aperture. The aluminum retainer included internal water flow passages that were used for either heating or cooling the wall assembly to desired temperatures. Fig. 6 shows a schematic of the experimental setup used for the spray vessel experiments. The *reference* mirror was used for Michelson interferometry and was removed for Fizeau interferometry.

The fuel used for these experiments was a multi-component E10 gasoline surrogate referred to as PACE20. PACE20 has been shown to closely match the spray dynamics of research-grade gasoline in free spray tests and the composition is provided by Karathanassis et al. [14]. Using a volume fraction-weighted average gives an estimated index of refraction of 1.408. This value was used for analysis of all spray vessel measurements. The injection duration used for spray vessel experiments was 680 µs electronic, resulting in a 780 µs hydraulic injection duration (except for the Michelson tests described below). An example of the resulting spray impingement footprint is shown by the Laser-Induced Fluorescence (LIF) image in Fig. 7. The red line indicates the linear probe region that is observed by the LCI system.

RESULTS AND DISCUSSION

Comparison of Michelson and Fizeau interferometry

To evaluate and compare the effectiveness of the two interferometry configurations, each was used in spray vessel measurements. For practical reasons, there were differences between the two implementations and the injection they observed. One key difference between the two interferometry implementations beyond the type of configuration used was the optical setup. The Michelson interferometry was performed with lower resolution imaging optics than the Fizeau configuration (32.8 µm projected pixel size vs. 11.6 µm projected pixel size) as described in the Methods section. This caused the Michelson system to be more susceptible to wash-out from corrugated film surfaces. Because of this and the reduced sensitivity due to dispersion effects that will be shown below, the Michelson setup could only detect thicker, flatter films. To accommodate this in the experiments, longer injection durations of 5 ms were used to produce thick, relatively stationary films. For these reasons, the two interferometry measurements will not be compared directly based on measurements of the same conditions. Instead, they will be compared based on the precision and accuracy that they could achieve in their respective test conditions and on other qualitative criteria related to feasibility. The results of the measurements used for comparison are shown in Fig. 8 at cold vessel conditions (20°C fuel, ambient gas, and transparent wall). Three different measurement timings are shown for an individual injection in each case. The shading axis was adjusted so that the minimum value was just above the noise floor so that real signals could be more easily distinguished.

As described in the previous section, fuel film thickness information is extracted from Michelson interferometry measurements by comparing the relative locations of the transparent wall and the film surface in the scattering potential. In the spray vessel experiments, refractive index matching precluded simultaneous observation of both the transparent wall and the film surface. After the spray impinges, only the film surface can be detected. The wall position was determined by measurements prior to impingement, as shown in the first frame of Fig. 8(a). The dashed red lines in Fig. 8(a) show the initial wall position. This wall indication cannot be considered completely reliable because an inspection of the intervening frames (not shown) suggests that there was significant recoil of the wall. There was an oscillation of the scattering potential peak on the order of 5 µm.

An important limitation of the Michelson approach in this spray vessel context is clear in Fig. 8(a). The dispersion compensation optics used in the *reference* path of the interferometer included replicas of the transparent wall, the vessel pressure window, and the beam splitter. Ideally, this would produce a perfect recreation of the dispersion experienced by the *sample* path in the *reference* path. However, small differences in the thickness of these pieces on the microscale, as well as angular misalignment and material imperfections, can compromise this compensation effect. It is clear in the results in Fig. 8(a) that the compensation is inadequate as the peak observed in the scattering potential is severely broadened. The peaks of the wall signal at 0 ms after Start of Injection (aSoI) have an average FWHM of 3.5 µm, far broader than the 0.94 µm limitation of the LED source. This impedes the ability to precisely extract a film thickness measurement from the scattering potential. Ultimately, the combined effects of dispersion and uncertainty in the wall location prevented film thickness measurements using the Michelson configuration.

For the Fizeau measurements, the relatively thin films caused the film thickness signal to exist near the DC component in the scattering potential. To allow for better identification of the film thickness, averaged images were subtracted from each frame prior to computing the Fourier transform. The averages were computed using the 100 frames before and the 100 frames after the frame being observed. Because the interference signal from the film is dynamic, it does not appear in the averaged frame, and so the average subtraction removes most of the DC signal while preserving the thickness information. All the Fizeau interferometry results shown in this section have the average subtraction applied to remove the DC component. Any remaining peak in the scattering potential then represents the film thickness.

The results of the Fizeau interferometry measurements are shown in Fig. 8(b). Initially at 0 ms aSoI, there is no signal observed because the spray has not reached the wall yet.

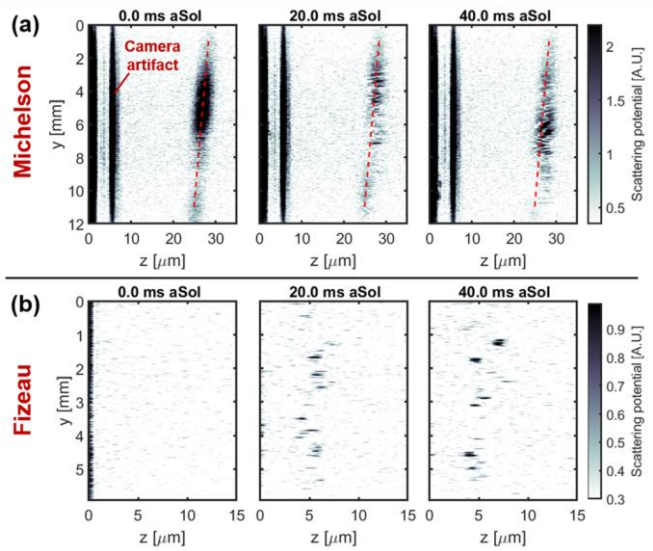

Fig. 8 Scattering potential plots measured in the spray vessel using: (a) Michelson interferometry (red dashed line shows wall position) (b) Fizeau interferometry.

Fizeau interferometry will only produce a signal when a film is present on the wall. At 20 ms aSoI, several pockets of signal are visible, indicating film thicknesses between 3 to 7 μm. Larger segments of identifiable signal are observed in the 40 ms aSoI frame. The intermittency of the signal, despite the entire probe line being covered by fuel, was caused by wash-out due to film surface corrugation. This is discussed more in the additional vessel measurements described below. The peaks observed in the scattering potential exhibit an average FWHM of 0.95 μm. This is approximately the resolution limit determined by the LED bandwidth. It demonstrates the capability of Fizeau interferometry to perform high-precision film thicknesses measurements in this high-speed configuration.

These tests expose several limitations of the Michelson approach that are avoided by the Fizeau configuration. While the refractive index matching issue in the Michelson interferometry configuration could be overcome, the dispersion issue is more significant. New compensation optics could be fabricated, but it would be expensive to ensure matching with vessel windows. Extremely precise alignment of the compensation windows would also be necessary to achieve proper correction because of their large thickness; small angular offsets lead to significant path length differences. There are post-processing techniques that have been used to mitigate dispersion effects [15]. However, such an approach introduces increased complexity into the data interpretation with little benefit outside of the stronger signal produced by the Michelson approach. Based on these observations, we conclude that Fizeau interferometry is superior to Michelson interferometry for film measurements in spray vessels with thick windows. If sufficient SNRs cannot be achieved with Fizeau interferometry, then a Michelson implementation may be considered. However, such a measurement will need to overcome significant challenges, including an accurate wall position measurement and, chiefly, dispersion correction. The remaining results presented in this work will focus on the Fizeau configuration to demonstrate and explore high-speed LCI in the spray vessel.

High-speed Fizeau interferometry of impinging sprays

The scope of this work is to demonstrate the capabilities of the high-speed LCI approach. In that spirit, example measurements are shown that illustrate the performance of the Fizeau LCI system, but a full quantitative analysis is not provided. Results are presented for two different temperature conditions: a "cold" vessel condition (20°C fuel, ambient gas, and transparent wall) and a "hot" vessel condition (90°C fuel, ambient gas, and transparent wall).

Cold spray vessel conditions

Under completely cold conditions, representative of the first several cycles of a GDI engine, vaporization of spray droplets and fuel films is minimal. This will tend to produce thicker films that persist for longer on combustion chamber surfaces. The cold vessel conditions are intended to represent this case.

The cold vessel results in Fig. 9 clearly show significant effects of wash-out as the interference signal is absent from most of the spatial locations. This is especially severe at earlier time points, such as the 16 ms example measurement where only a few spots of reflected signal can be seen. This is due to corrugation of the fuel film surface, which is expected to be most severe immediately after deposition and improve as the film smooths with time. This is consistent with the observations here, as there are more spots of recorded signal at the two later timings in Fig. 9. Though it limits the amount of quantitative film thickness data that can be collected, the absence of signal in areas that are known to be wetted (confirmed by a drop in reflectivity after liquid impact) indicates the magnitude of corrugation, or "roughness", of the film's surface. It can be inferred that the areas where signal is absent are inclined at angles greater than that of the $\alpha_{\max}$ of the LCI system (estimated to be 0.96°). The points where strong signal is observed are likely local minima or maxima of the film, which can be informative when interpreting results. The throughput of film thickness measurements of the system can be improved by increasing the spatial resolution of the imaging optics. The achievable spatial resolution of this system was limited by the illumination intensity and SNR constraints.

The places where measurable signal is observed provide insight into the morphology and dynamics of the film. At 16 ms aSoI, the film was highly corrugated and the observed film thicknesses fall between 6 to 9 μm. As described above, these points of signal are likely local extrema of the film thickness, and so it suggests that most of the film existed within this range of thicknesses at that moment. Later, in the 50 and 85 ms aSoI timing cases, signal is observed over a greater extent of the film. This indicates that the film had settled into a less corrugated

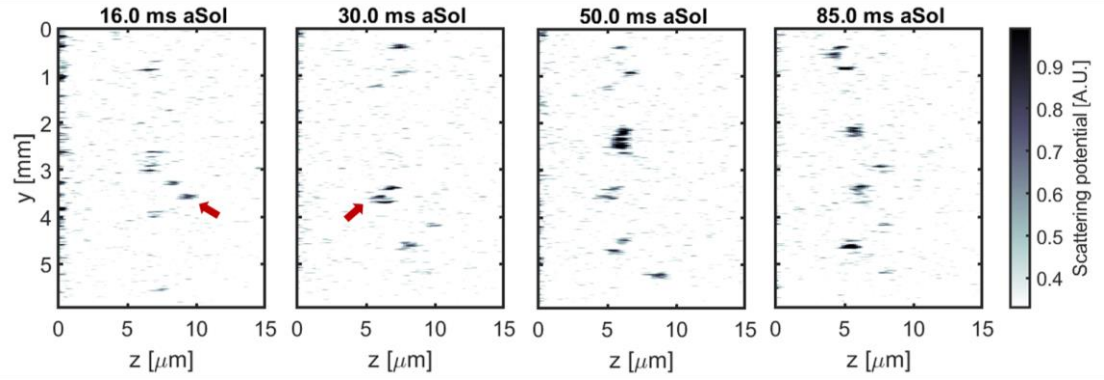

Fig. 9 Measured scattering potentials showing film thicknesses in the "cold" vessel conditions at various times after injection. Red arrows highlight dynamic changes in film thickness captured by LCI.

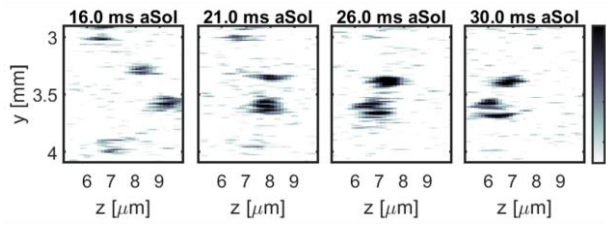

Fig. 10 A closeup series of frames showing the film thinning process highlighted in Fig. 9.

state. The film was also thinner at 85 ms aSoI, with thicknesses observed between 4 to 8 µm. It is not possible to determine the cause of reduced film thicknesses from LCI measurements alone. However, it can be intuitively reasoned that the film thinning was due to a combination of evaporation and surface tension effects redistributing the film over a wider extent of the wall surface. By the end of observation (10 ms aSoI) a significant film remained on the wall in this cold temperature case.

The example film thickness measurement in Fig. 9 provides a demonstration of the capability of this high-speed LCI system to resolve dynamics of the fuel film. The red arrows in the 16 ms aSoI and 30 ms aSoI indicate fuel thickness observations at the same spatial position. Initially, the film was 9.3 µm thick at this location, and after the 14 ms interval, the film measures 6.0 µm thick at that same location. Fig. 10 provides additional intervening frames focused on the transition of this point in the film from a thick to thinner state. The 140 frames that were captured in this interval smoothly resolve this thinning process. This type of observation is only possible through kHz-rate single-shot measurements, such as those enabled by this system.

Hot spray vessel conditions

After an engine has been fired for several cycles, the combustion chamber surfaces and cylinder head begin to heat up. Toward the end of what is called cold start, the gas inside the cylinder, the fuel being injected, and the surface of the piston all reach elevated temperatures. These increased temperatures increase droplet vaporization, leading to less fuel impinging on surfaces and deposited into films. The high temperatures are also expected to increase the evaporation rate of fuel film. The "hot" vessel case is intended to represent this situation.

Fig. 11 shows example film measurements from the hot vessel condition. As expected, the fuel film was less thick for this condition compared to the cold results at all temporal points. Peaks in the scattering potential are visible between 1 µm and 4 µm at 20 ms aSoI, early after fuel deposition. This film was significantly thinner than the film in the cold vessel case, as expected. This can be attributed to a reduced liquid fuel volume impinging on the wall due to increased evaporation of the fuel in the spray at these higher temperatures. It should also be noted that at all observation timings, there are more locations producing measurable signal than for the cold vessel condition. This suggests that the film surface was less corrugated in the hot case than the cold case, leading to

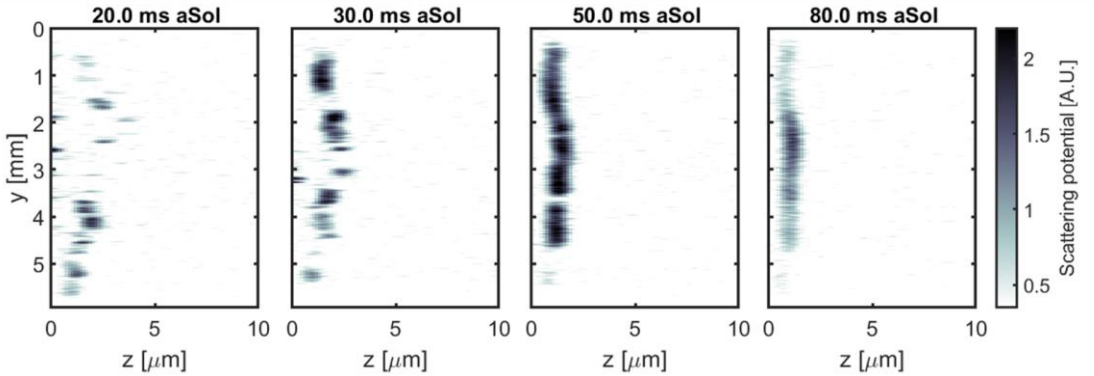

Fig. 11 Measured scattering potentials showing film thicknesses in the "hot" vessel conditions at times after injection.

less signal wash-out. This is consistent with expectations of reduced surface tension at increased temperatures. By 50 ms aSoI in the hot case, the majority of spatial locations were producing measurable signal, and the film thickness over that range varies by less than 1 μm. This shows that the late film in the hot case exhibited a high degree of flatness and the film was evenly distributed.

The dynamics of the film in the hot vessel case can be characterized as a consistent thinning of the film over the duration of observation. Like the cold vessel case, this is likely driven by both evaporation and redistribution of the fuel over a wider area. It is expected that the elevated temperature of the hot vessel cases creates significantly more evaporation than in the cold case. The recession of the film leads to almost complete elimination of the film over the 100 ms duration of measurement in the hot vessel case. By 100 ms aSoI the film is either undetectable or less than 1 μm at all locations.

CONCLUSIONS

Spectral LCI can be used for high-speed measurements of fuel film thickness under engine-relevant conditions. Measurements of impinging GDI sprays were carried out in a constant volume spray vessel under conditions representative of engine cold start. Spectral LCI measurements at 10 kHz were able to quantify film thickness and observe dynamics of the evaporating film. The measurements achieved a thickness resolution of 0.95 μm over a one-dimensional spatial extent of 6 mm across the surface of the film. The system was able to first detect film thickness 6 ms after start of injection and experienced intermittent signal due to film corrugation. Improvements in imaging resolution would increase data throughput.

The Fizeau configuration is more effective than the Michelson configuration for measurements in enclosed spray chambers. It becomes difficult to fully correct for dispersion effects in the presence of thick pressure windows. This causes a significant loss in thickness resolution with Michelson interferometry. Also, the recoil of the transparent wall in response to spray impingement caused significant movement on micrometer scales so that the precise position of the wall could not be known during injection tests. This precluded the use of Michelson interferometry in the case of refractive index matching between the wall material and the fuel. For these reasons, the Fizeau configuration was the superior choice in these high-speed environments.

Pulsed white phosphor LEDs were effective light sources for high-speed spectral LCI measurements. The broad illumination spectrum of the white LEDs used in this work provided sufficient bandwidth (approximately 150 nm) to enable high-resolution film thickness measurements. Pulsing at the highest achievable duty cycle (15% at 10 kHz) provided adequate SNRs for single-shot measurements. To achieve this high duty cycle required sub-ambient cooling of the LED package to minimize the occurrence of thermal failure. While white LEDs were capable illumination sources, future work may explore other broadband sources that might be able to improve both SNRs and maximum acquisition rates. A possible candidate light source is supercontinuum lasers that have been previously used in other LCI applications [16]. They provide a very large spectral bandwidth, and their spatially coherent emission can be leveraged to increase illumination intensities and resulting SNRs.

Acknowledgements
The authors would like to thank Aaron Czeszynski for designing the TEC thermal solution and the wall retainer. They would also like to thank Meghna Dhanji for assistance running the experiments. Sandia National Laboratories is a multi-mission laboratory managed and operated by National Technology and Engineering Solutions of Sandia, LLC., a wholly owned subsidiary of Honeywell International, Inc., for the U.S. Department of Energy's National Nuclear Security Administration under contract DE-NA0003525. This paper describes objective technical results and analysis. Any subjective views or opinions that might be expressed in the paper do not necessarily represent the views of the U.S. Department of Energy or the United States Government.

REFERENCES

[1] Drake, M.C., Fansler, T.D., Solomon, A.S., Szekely, G.A., SAE Trans. 112:762 (2003).
[2] Stevens, E., Steeper, R., SAE Trans. 110:1287 (2001).
[3] Miyashita, K., Tuskamoto, T., Fukuda, Y., Kondo, K., Aizawa, T., SAE 2016-01-2165 (2016).
[4] Song, B.H., Choi, Y.H., Journal of Mech. Sci. and Tech. 22(12):2526 (2008).
[5] Lin, M.-T., Sick, V., SAE 2004-01-1355 (2004).
[6] Schulz, F., Schmidt, J., Beyrau, F., Exp. Fluids 56:98 (2015).
[7] Porter, J.M., Jeffries, J.B., Hanson, R.K., Appl. Phys. B, 102:345 (2011).
[8] Shway, K., Bardi, M., Bruneaux, G., Kaiser, S., ICLASS, Edinburgh (2021).
[9] Borgetto, N., Galizzi, C., André, F., Escudié, D., Exp. Therm. And Fluid Sci. 44:512 (2013).
[10] Schumacher, L., Seel, K., Reddemann, M.A., Kneer, R., Rev. of Sci. Instruments 89:113703 (2018).
[11] Fercher, A.F., Drexler, W., Hitzenberger, C.K., Lasser, T, Rep. Prog. Phys. 66:239 (2003).
[12] https://ecn.sandia.gov/diesel-spray-combustion/sandia-cv/combustion-vessel-geometry/2009-to-present/
[13] Kim, N., Vuilleumier, D., Sjoberg, M. SAE 2021-01-0544 (2021).
[14] Karathanassis, I., White, L., Koukouvinis, P., Hwang, J., Pickett, L.M., Gavaises, M., ICLASS, Edinburgh (2021).
[15] Hillman, D., Bonin, T., Lührs, C., Franke, G., Hagen-Eggert, M., Koch, P., Hüttmann, G., Opt. Exp. 20(6):6761 (2012).
[16] Brown, W., Kim, S., Wax, A., J. Opt. Soc. Am. A 31(12):2703 (2014).